Supplementary Material

Ionic Coulomb Blockade and the Determinants of Selectivity in the NaChBac Bacterial Sodium Channel

O. A. Fedorenko, I. Kh. Kaufman, W. A. T. Gibby, M. L. Barabash, D. G. Luchinsky, S. K. Roberts, P. V. E. McClintock

S1. Electrophysiology

Table S1. Oligonucleotides containing the sequence for the desired amino acid substitutions used in this study.

Amino acid sequence	Nominal *Qf*	Template	Forward primer	Reversed primer
L**A**SWAS	0	LESWAS	GGTCACGCTAgccTCATGGGCGAGcggcg	ACTTGGAACAATGTTAACAAACtaagc
LE**K**WAS	0	LESWAS	CACGCTAGAGaagTGGGCGAGCG	ACCACTTGGAACAATGTTAAC
L**D**SWAS	-4	LESWAS	GGTCACGCTAgatTCATGGGCGAG	ACTTGGAACAATGTTAACAAACTAAGC
LE**E**WAS	-8	LESWAS	CACGCTAGAGgagTGGGCGAGCG	ACCACTTGGAACAATGTTAAC
LE**D**WAS	-8	LESWAS	CACGCTAGAGgatTGGGCGAGCG	ACCACTTGGAACAATGTTAAC
L**DE**WAS	-8	LEEWAS	GGTCACGCTAgatGAGTGGGCGA	ACTTGGAACAATGTTAACAAACTAAGCTG
L**DD**WAS	-8	LEDWAS	GGTCACGCTAgatGATTGGGCGA	ACTTGGAACAATGTTAACAAACTAAGC

Whole-cell voltage clamp recordings were performed at room temperature (20◦ C) using an Axopatch 200A (Molecular Devices, Inc.) amplifier. Whole cell currents were elicited by a series of step depolarizations (+95mV to -85mV in -15mV steps) from V_{hold} = -100mV. Representative examples of currents recorded under such conditions, mediated by wild type and mutant NaChBac channels, are shown on Figure S0

Whole-cell rather than single-channel recordings are used in the interests of precision, based on the larger and more easily measurable currents. The amplitude of a single NaChBac channel is only about 2 pA in 140 mM Na solution, so if the permeability of a channel decreases two-fold or even more in solutions with other tested cations, it would be difficult to detect the currents and obtain reliable values for conductances. The whole cell peak currents of wild type NaChBac in 140 mM Na solution have amplitudes of 1-2 nA, which enables us to perform reliable recordings. Whole-cell currents are the product of the number of channels, the open probability and the single channel conductance. Because the number of expressed channels is constant for a given cell, and the open probability does not change with a change of the tested cation in solution, the difference in conductance observed is proportional to the change in single channel conductance.

Patch-clamp pipettes were pulled from borosilicate glass (Kimax, Kimble Company, USA) to resistances between 2-3 MOhm. Pipette solution was either PS1 (120mM Cs-methanesulfonate, 20mM Na-gluconate, 5mM CsCl, 10mM EGTA, and 20mM HEPES, pH7.4 adjusted with 1.8mM

CsOH) or Cs-free PS2 (15mM Na-gluconate, 5mM NaCl, 90mM NMDG, 10mM EGTA, and 20mM HEPES, pH7.4 adjusted with 3mM HCl). Unless otherwise stated, GOhm seals were obtained in standard bath solution (SBS_{Na}; 140mM Na-methanesulfonate, 5mM CsCl, 10mM HEPES and 10mM glucose, pH=7.4 adjusted with 4.8mM CsOH). For experiments with LDDWAS and LDEWAS, Cs-free SBS_{Na} (SBS_{Nax}: 132mM Na-methanesulfonate, 5mM NaCl, 10mM HEPES and 10mM glucose, pH=7.4 adjusted with 3.6mM NaOH) was used; these channels are permeable to Cs and thus its removal from the test solutions was required to establish pseudo-bionic conditions (Fig. S1). Furthermore, the bath solutions (SBS_{Nax} and SBS_{Nax} in which 140 mM Na^+ was replaced with the test monovalent cation) used for recording LDDWAS activity in the presence of extracellular monovalent cations also contained 10 mM EGTA (see below) to account for the high affinity Ca2+ blockade of the channel.

Permeability to different test cations was determined by replacing 140mM NaCl with equimolar test monovalent cation or 100mM test divalent cation using Cl- salts. Permeability ratios (P_x/P_{Na}) were determined from whole cell current reversal potentials (E_{rev}) for monovalent/divalent cations according to [34, 35]. The effective activity coefficients were calculated using the Debye-Hűckel equation (Table S2).

In experiments with varied Na/Ca mixtures, GOhm seals were first obtained in SBS_{Na} (or SBS_{Nax} for experiments with LDDWAS and LDEWAS) containing 10 nM $[Ca^{2+}]_{free}$, and the bath solution replaced with solutions containing increasing concentrations of Ca^{2+}. Different chelators were used to fix Ca2+ concentration as needed, for details see Table S3., and HEDTA to fix Ca2+ concentrations at 10 μM, 100 μM and 1 mM. $[Ca^{2+}]_{free}$ were calculated using Webmaxc (ttp://web.stanford.edu/cpatton/webmaxcs.htm). Na^+ and Ca^{2+} (for 10mM, 50mM and 100mM) activities were calculated using the Debye-Hickel equation (we consider $[Ca^{2+}]_{free}$ = ion activity of Ca^{2+}); for details see Table S2.

Osmolarities of all solutions were measured using a Wescor vapor pressure osmometer (model 5520) and adjusted to 280 lmOsmKg-1 using sorbitol. All solutions were filtered with a 0.22mm filter before use. Whole cell currents were recorded 3 minutes after obtaining whole cell configuration to ensure complete equili- bration of the pipette solution and cytosol. The bath solution was grounded using a 3 M KCl agar bridge; the liquid junction potential, determined experimentally [36], agreed with that calculated (using JPCalc program, Clampex, Axon Instruments, Inc.), were less than 2.6mV, and were not accounted for.

The recording chamber volume was approximately 200 μl and was continuously exchanged by a gravity-driven flow/suction arrangement at rate of ≈2ml/min; to ensure complete exchange of bath solution. Electrophysiological recordings were initiated after >4 minutes of continuous solution change.

Results were analysed using Clampfit 10.1 software (Molecular Devices) and Origin 9.1 (OriginLab). Data are presented as Mean (± SEM) (n), where n is the number of independent experiments.

Table S2. Concentrations and the effective activity coefficients of solutions used for permeability ratios determination.

	Na^+	**Li^+**	**K^+**	**Rb^+**	**Cs^+**	**Mg^{2+}**	**Ca^{2+}**	**Sr^{2+}**	**Ba^{2+}**
Concentration (in mM)	**140**	**140**	**140**	**140**	**140**	**100**	**100**	**100**	**100**
activity coefficients (Debye-Hückel equation)	0.74	0.78	0.72	0.71	0.71	0.34	0.29	0.25	0.25
Free concentrations/ activities	103.6	109.2	100.8	99.4	99.4	34	29	25	25

Table S3. Total and free concentrations, which correspond to ion activities, for the mixed Na^+ and Ca^{2+} solutions in our AMFE experiments (*only for LDDWAS and LDEWAS mutant channels).

Solutions (total concentrations)			**Free concentrations/ ion activities**	
Na^+	Ca^{2+}	Chelator	Na^+	Ca^{2+}
140 mM	0.23mM	12 mM EGTA+ 10 mM BAPTA*	110.6 mM	0.12nM*
140 mM	0.23mM	12 mM EGTA	110.6 mM	1.5 nM
140 mM	0.23mM	3mM EGTA	110.6 mM	6.4 nM
140 mM	0.23mM	2 mM EGTA	110.6 mM	10 nM
140 mM	0.85mM	2 mM EGTA	110.6 mM	100 nM
140 mM	1.76mM	2 mM EGTA	110.6 mM	1 μM
140 mM	0.69 mM	1 mM HEDTA	110.6 mM	10 μM
140 mM	1.05 mM	1 mM HEDTA	110.6 mM	100 μM
138 mM	2 mM	1 mM HEDTA	108.7 mM	1 mM
130 mM	10 mM		101.0 mM	4.13 mM

70 mM	50 mM		52.2 mM	18.3 mM
40 mM	100 mM		28.4 mM	31.7 mM

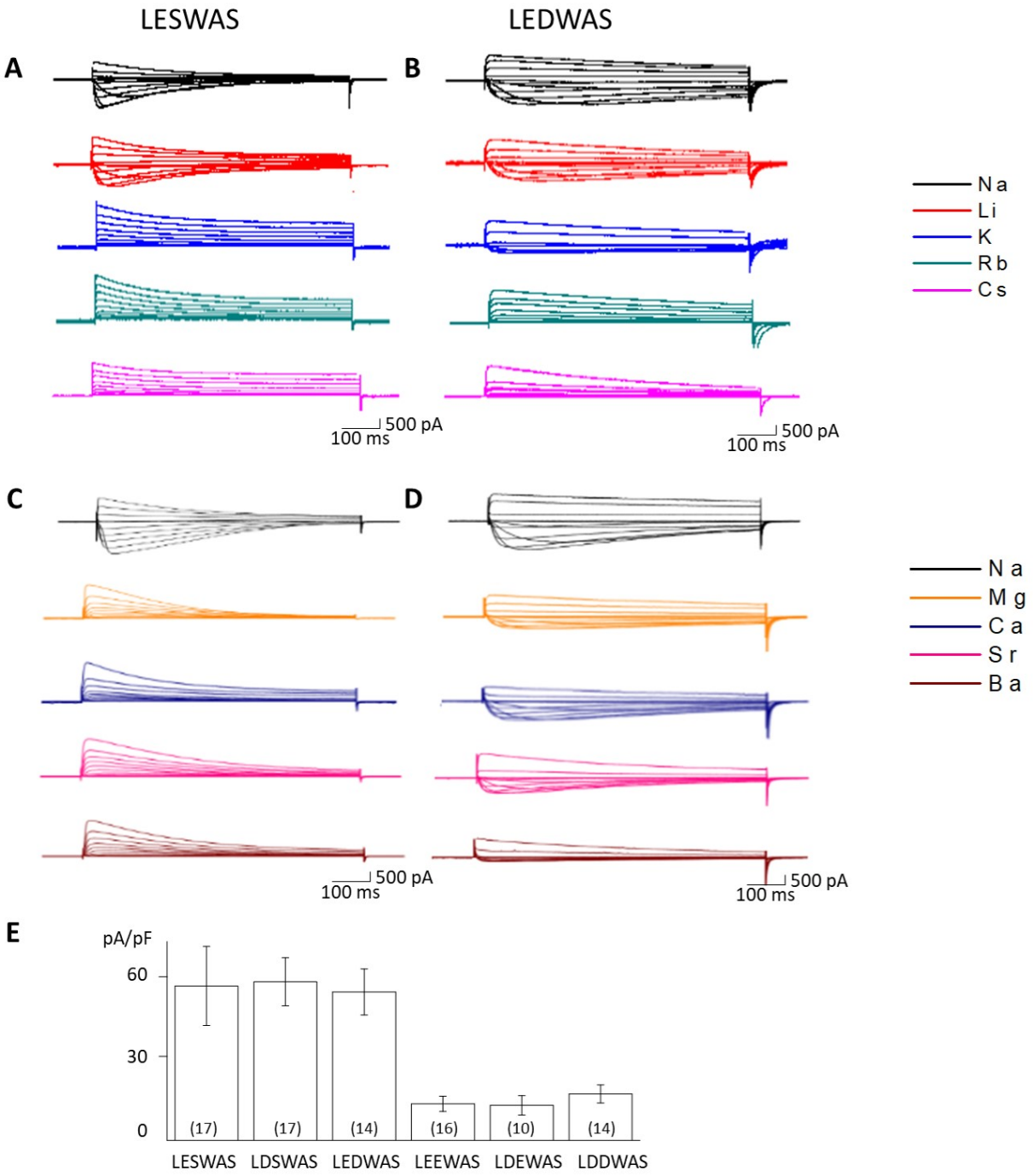

Figure S0. Examples of raw experimental measurements of monovalent (A, B) and divalent (C, D) ionic currents mediated by wild type LESWAS (A, C) and mutant LEDWAS (B, D) NaChBac channels as functions of time following step depolarisations. The sodium currents, used for normalisation purposes, are shown in panel E.

S2. Experimental results of mutant studies of NaChBac

Table S4. Reversal potentials (E_{rev}), permeability ratios (P_X/P_{Na}) and the relative peak inward current (I_X/I_{Na}) for the tested cations for the channels with Q_f = -4 and Q_f = -8. All values are means (± SEM) with the number of experiments in parenthesis. E_{rev} is the mean reversal potential in millivolts measured for each cation; in cases where inward current was not detected, estimated values for E_{rev} were determined as voltage at which outward current could be detected. Permeability ratios (P_X/P_{Na}) for each cation were calculated (see in Methods) from paired changes in E_{rev} measured for a given cell perfused first with control Na^+ solution and after replacement with the test cation solution according to the following equations (*Hille, 1972*; *Sun et al., 1997*) for monovalent cations:

$P_X/P_{Na} = \alpha Na_i/\alpha X_e\ [\exp(\Delta E_{rev}/(RT/F))]$,

and divalent cations:

$P_Y/P_{Na} = \{\alpha Na_i\ [\exp(E_{rev}\ F/RT)][\exp(E_{rev}\ F/RT)+1]\}/4\alpha Y_e$,

where ΔE_{rev} is the change in reversal potential on replacing Na^+ with the tested cation, α is the activity coefficients for the ion (i, internal and e, external), R - the universal gas constant, T - absolute temperature, and F - the Faraday constant. The effective activity coefficients (αx) were calculated using the Debye-Hückel equation and are listed in Supplemental Table 2. I_X/I_{Na} was measured as the ratio of maximum peak inward current observed for the test cation to that for observed Na^+ in the same cell.

		LESWAS	LDSWAS	LEEWAS	LDEWAS	LEDWAS	LDDWAS
Li^+	E_{rev}	48.7±1.42 mV (n=6)	42.3±1.8 mV (n=6)	47.9±0.4 mV (n=9)	43.3±2.1 mV (n=6)	48.2±1.57mV (n=6)	42.3±0.7 mV (n=7)
	P_{Li}/P_{Na}	0.8	0.6	0.7	0.6	0.8	0.6
	I/I_{Na}	0.8	0.6	0.7	0.9	0.7	1
Na^+	E_{rev}	51.0 ±1.26 mV (n=17)	49.0±1.0 mV (n=21)	51.8±1.1 mV (n=16)	47.8±1.4 mV (n=10)	50.2±0.81mV (n=14)	46.4±1.0 mV (n=14)
	P_{Na}/P_{Na}	1	1	1	1	1	0.9

	I/I_{Na}	1	1	1	1	1	1
K^+	E_{rev}	<-30 mV (n=8)	42.5±2.4 mV (n=5)	-15.9±3.8 mV (n=7)	43.4±3.1 mV (n=7)	9.7±2.31 mV (n=8)	48.5±0.6 mV (n=7)
	P_K/P_{Na}	<0.1	0.8	<0.1	0.8	0.2	1
	I/I_{Na}	<0.1	0.6	<0.1	0.8	0.1	1.2
Rb^+	E_{rev}	<-30 mV (n=5)	-8.8±6.0 mV (n=5)	-22.9±4.7 mV (n=6)	10.3±1.5 mV (n=5)	-7.9±1.57 mV (n=6)	35.9±4.1 mV (n=7)
	P_{Rb}/P_{Na}	<0.1	0.1	<0.1	0.2	0.1	0.6
	I/I_{Na}	<0.1	<0.1	<0.1	0.1	<0.1	0.2
Cs^+	E_{rev}	<-30 mV (n=5)	-29.0±5.0 mV (n=5)	-40.4±6.7 mV (n=6)	-3.9±3.1 mV (n=5)	-11.8±7.42 mV (n=6)	8.2±1.1 mV (n=7)
	P_{Cs}/P_{Na}	<0.1	<0.1	<0.1	0.1	0.1	0.2
	I/I_{Na}	<0.1	<0.1	<0.1	0.1	<0.1	<0.1
Mg^{2+}	E_{rev}	-26.3±9.24mV (n=5)	19.0±3.0 mV (n=6)	-3.9±2.2 mV (n=6)	15.9±7.4 mV (n=5)	49.5±1.78 mV (n=6)	Block (n=15)
	P_{Mg}/P_{Na}	0.1	0.7	0.2	0.6	6.5	-
	I/I_{Na}	<0.1	<0.1	<0.1	0.1	0.2	-
Ca^{2+}	E_{rev}	-5.1±2.63 mV (n=9)	53.3±1.2 mV (n=7)	58.7±1.8 mV (n=9)	block	71.5±1.26 mV (n=11)	Block (n=16)
	P_{Ca}/P_{Na}	0.2	10.2	14.1	-	41.1	-
	I/I_{Na}	<0.1	0.4	0.25	-	0.4	-
Sr^{2+}	E_{rev}	<-30 mV (n=5)	54.8±2.1 mV (n=6)	45.0±3.8 mV (n=7)	75.8±1.8 mV	59.2±4.34 mV (n=7)	Block (n=15)

					(n=7)		
	P_{Sr}/P_{Na}	<0.1	13.2	8.5	66.8	18.5	-
	I/I_{Na}	<0.1	0.4	0.2	0.3	0.3	-
Ba^{2+}	E_{rev}	<-30 mV (n=5)	40.9±3.8 mV (n=6)	13.4±0.8 mV (n=8)	61.6±2.5 mV (n=5)	49.0±1.98 mV (n=9)	Block (n=15)
	P_{Ba}/P_{Na}	<0.1	4.7	0.7	22.2	8.5	-
	I/I_{Na}	<0.1	0.2	<0.1	0.1	0.1	-

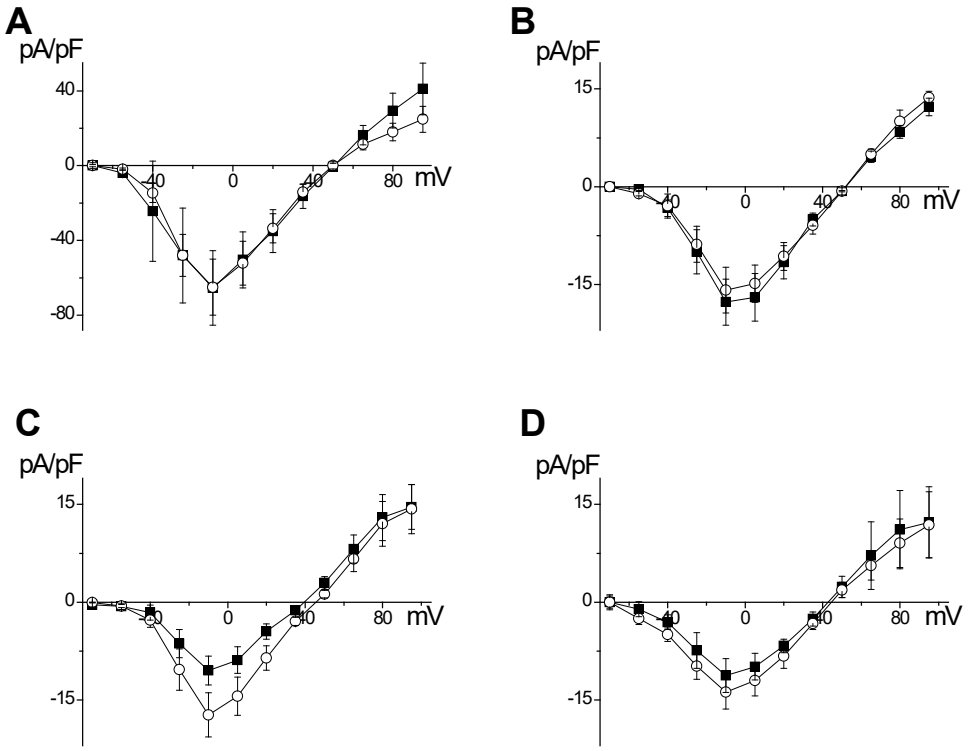

Figure S1. Optimising the pipette solution. Plot of average peak current (I_{peak}) density against test voltage from cells expressing LDSWAS (A; ■ - n =10; ○ - n = 15; note the scale); LEEWAS (B; ■ - n =16; ○ - n = 7), LDDWAS (C; ■ - n =7; ○ - n = 14) and LDEWAS (D; ■ - n =10; ○ - n = 10) mutant channels recorded in SBS_Na_x and PS1 (■) or PS2 (○) in response to test voltages ranging from +95 mV to -70 mV (in -15 mV steps) from V_{hold} -100 mV. Note that for LDDWAS (and, to a lesser extent, LDEWAS) the removal of Cs^+ (○) from the pipette solution resulted in a shift in E_{rev} and larger inward current consistent with Cs^+ permeation.

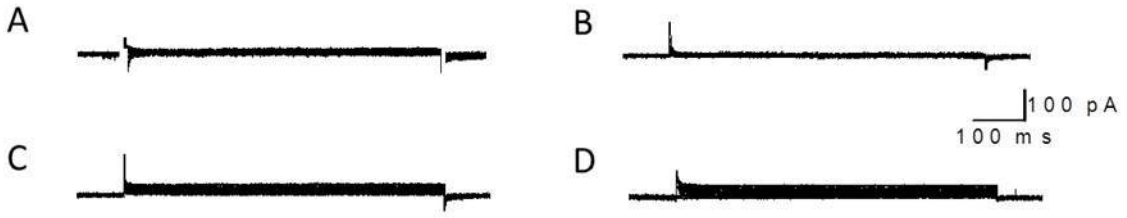

Figure S2. Original traces for LASWAS (A, B) and LEKWAS (C, D) mutant channels recorded in the bath solution (SBS_{Na})containing 140 mM NaCl (A, C) or in 100 mM $CaCl_2$ solution (B, D) and PS1 in response to test voltages ranging from +95 mV to -70 mV (in -15 mV steps) from V_{hold} -100 mV.

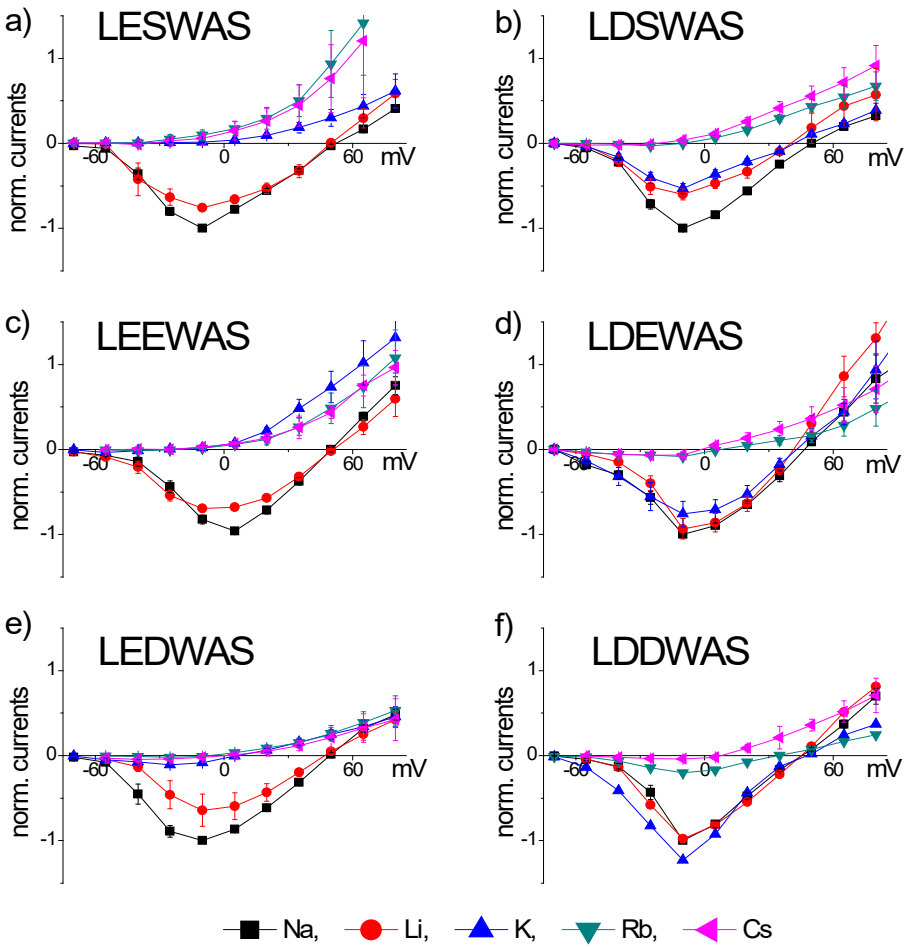

Figure S3. Monovalent cation permeability. Mean peak current voltage relationships for wild type NaChBac LESWAS (a), LDSWAS (b), LEEWAS (c), DEWAS (d), LEDWAS (e) and LDDWAS (f) mutant channels for Na^+, Li^+, K^+, Rb^+ and Cs^+ (as labelled) were determined by normalising peak current magnitudes recorded in Na^+ bath solution from the same cell prior to replacement of extracellular Na^+ for test cation. Averages (±SEM) are from at least 5 cells.

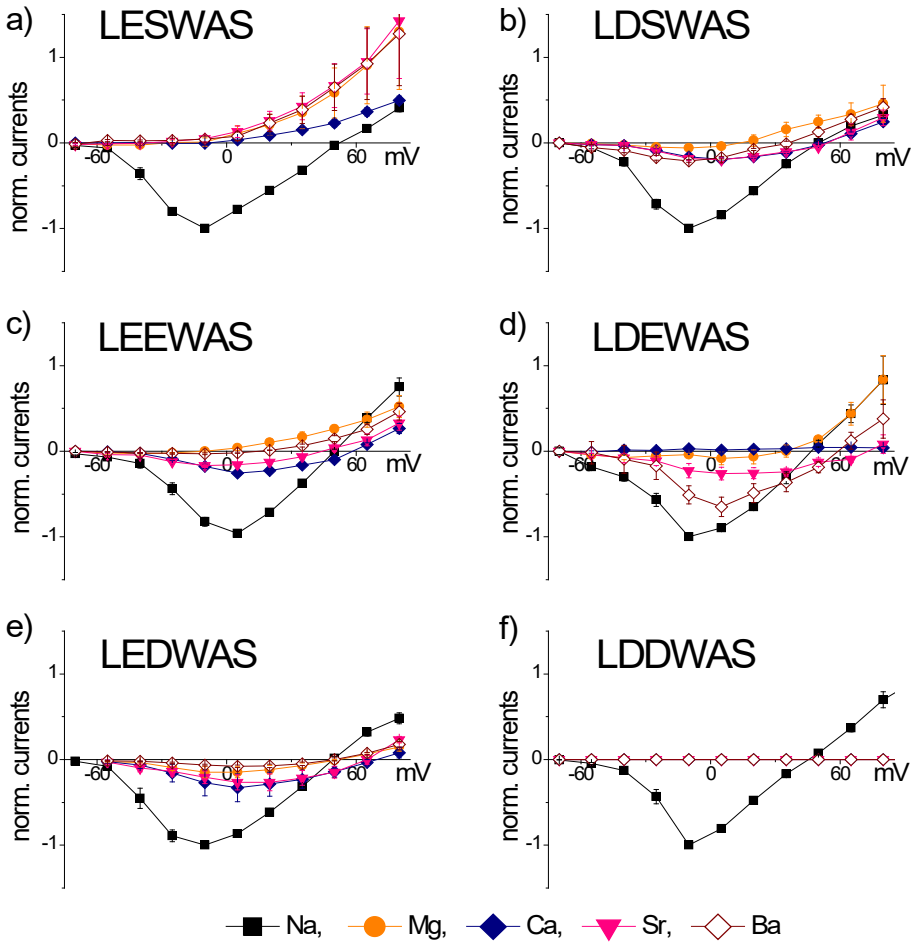

Figure S4. Divalent cation permeability. Mean peak current voltage relationships for wild type NaChBac LESWAS (a), LDSWAS (b), LEEWAS (c), LDEWAS (d), LEDWAS (e) and LDDWAS (f) mutant channels for Na^+ (for comparison), Mg^{2+}, Ca^{2+}, Sr^{2+} and Ba^{2+} (as labelled) were determined by normalising peak current magnitudes recorded in Na+ bath solution from the same cell prior to replacement of extracellular Na^+ for test cation. Averages (±SEM) are from at least 5 cells.

.

S3. Models and theories

Despite their small size, ion channels are complicated objects made up of thousands of atoms each of which interacts with all of the others, with water, and with any ions that are within the channel's pore or nearby. In practice, before physics can usefully be applied, some simplification is needed, and there are several different levels on which channels can be modelled. The features and mechanisms of the electro-diffusive ionic motion have been the subject of numerous theoretical and simulation-based studies, performed with very different scales, models and methods [1, 2], including (in order of decreasing model detail) all-atom molecular dynamics (MD) simulations [3], mesoscopic Brownian dynamics (BD) simulations [2, 4], Monte-Carlo simulations [5], and Poisson-Nernst-Planck (PNP) simulations [6]. The different models represent different physical scales and provide complementary information. Here, we are mainly interested in the BD level, but with some illumination from MD modelling. To set the context, we now consider briefly the advantages and disadvantages of the latter two approaches.

Molecular dynamics modelling ignores electronic degrees of freedom but, in principle, considers all interactions contributing to the net force on each component particle and takes explicit account of individual water molecules. The atoms are usually treated as point particles, but with inclusion of hard-core repulsive forces to model the atomic radii. Sometimes, particular groups of atoms far from the pore are assumed to move together as single units in order to simplify and accelerate the computation. The main advantages of MD modelling lie in its conceptual simplicity and its inclusivity of all the different interactions, and it is often considered as the *de facto* standard for nanoscale research, quite generally, as well as for research on ion channels. It can be used to confirm the atomic structure of the channel protein, as well as to model the permeation process. Its main disadvantage is that the detailed character of the computations makes them very demanding in terms of computational resources so that, even using supercomputers and massive parallelism, it is currently seldom impossible to run the simulations for long enough to produce statistically meaningful currents for comparison with experiment. An important consequence is that MD cannot identify emergent phenomena at a higher level, for example ionic Coulomb blockade (ICB).

Unlike MD simulations [2], the BD model takes no account of the detailed atomic structure of the protein or residues. Rather, it treats the water and protein as continuum dielectrics with their bulk dielectric constants; unlike PNP theory, however, it takes explicit account of the charge/entity discreteness of the ions. Simplified electrostatically-controlled self-consistent BD models of this kind have already shown their utility for describing relatively wide calcium/sodium channels [4, 5, 7–9]. They can be applied to e.g. TRP channels [10], to biomimetic nanotubes [11, 12], and to other artificial pores. The model is summarised below in section S3.1. Further details together with a fuller discussion of its validity and limitations, have been given elsewhere [9, 13, 14]. Its great advantage lies in computational speed, so that it is feasible not only to determine the permeating current with good statistics, but to do so under a wide range of different conditions, e.g. for different membrane potentials and ionic concentrations, as well as for different mutants.

As in the main paper, with SI units, ε_0 is the permittivity of free space, e is the elementary charge, z is the ion valence, k_B is Boltzmann's constant and T is the temperature. We use the conventional shorthand symbols for amino acid residues: Alanine (A); Aspartate (D, with $Q = -1|e|$); Glutamate (E, with $Q = -1|e|$); Leucine (L); Lysine (K, with $Q = +1|e|$); Serine (S); Threonine (T); Tryptophan (W); and so on, where A, L, S, T, and W are all uncharged.

S3.1. Self-consistent electrostatic & Brownian dynamics model

The generic electrostatic/BD model describes the SFs of calcium/sodium ion channels. It treats the channel's SF as a water-filled, cylindrical, negatively-charged pore in the protein, radius $R_c \approx 0.3$nm and length $L \approx 1$nm. Such simple models have been widely and successfully used in earlier research [4, 7, 15, 16] to describe the permeation of small metallic cations. The model is shown schematically in Fig. S5(a). The x-axis is coincident with the channel axis and $x = 0$ in the center of channel. The charged residues are modelled as a symmetrically-placed, uniformly-charged, rigid ring $R_Q \leq R_c$ of negative charge $|Q_f| = (0 - 8)e$. We

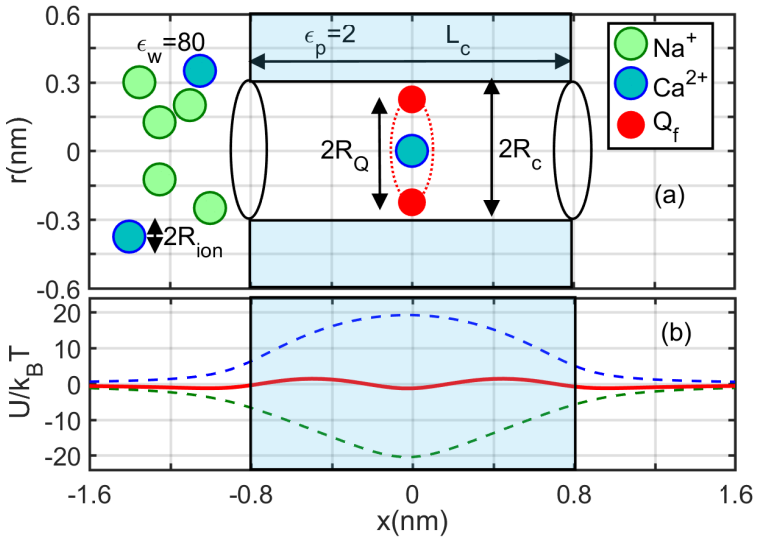

Figure S 5: Electrostatic model of the selectivity filter (SF) of a Ca^{2+} or Na^+ channel. (a) The model represents the SF as a negatively-charged, axisymmetric, water-filled, cylindrical pore of radius $R_c \approx 0.3$nm and length $L_c \approx 1.6$nm through the protein hub in the cellular membrane. The protein is pale-blue-shaded and the water is colourless. The fixed charge Q_f is modelled as a single charged ring of radius R_Q, shaded in red; in the present manuscript we take no account of the possible difference in radii of the channel and the charge ring, but assume that $R_q = R_c$. (b) Energetics of a moving Ca^{2+} ion for a fixed charge $Q_f = -1e$. The dielectric self-energy barrier U_q^{SE} (dashed blue line) is balanced by the site attraction U_{qQ} (dashed green line) resulting in an almost barrier-less energy profile U_b (red solid line). (Modified from [24])

take both the water and the protein to be homogeneous continua with dielectric constants $\varepsilon_w = 80$ and $\varepsilon_p = 2$, respectively. Despite its simplicity, the model allows one to predict/explain some essential features of conduction and selectivity and, in particular, valence selectivity [17] including ICB effects [7, 14, 18]; as mentioned above, the model was recently extended to account for local binding [19].

Fig. S5(b) illustrates the phenomenon of resonant barrier-less conduction, which is typical of electrostatic models. It arises when the energy of the ion-site attraction U_{qQ} balances the dielectric self-energy (or more generally, the dehydration) barrier U_q^{SE}. Resonant barrier-less conduction is key to the understanding of selectivity in ion channels [9, 14, 20, 21]. Selectivity arises because different ion species exhibit different barrier heights and site affinities, and have different dependences of these parameters on Q_f and ionic radii.

The model supposes that ion transport through the SF is controlled by coupled Poisson electrostatic and Langevin stochastic equations [2, 4] i.e. that we can implement self-consistent Brownian dynamics (BD) simulations of ion transport. Single-file ionic motion is assumed for Ca^{2+} and Na^+ channels. The BD simulations are based on numerical solution of the 1D over-damped, time-discretised, Langevin equation for the i-th ion. A parametric study [13] showed that the results are robust to small variations in the geometrical parameters of the SF.

As in the case of other simplified models, we make use of *effective values* of many model parameters, such as R, L, ε_w, ε_p and, particularly Q_f. The concept of effective values allows one to use very generalised models far outside their range of rigorous validity, e.g. for more complicated geometry of the SF. The *effective charge* [9, 22, 23] Q_f^* was introduced as a fitting parameter to optimise agreement of the model with theoretical or experimental data. The physical nature of Q_f^* depends on the particular model used, and on the channel structure, and Q_f^* may differ from Q_f^{nm} on account of e.g. the dipole moment of the molecule, screening, or site protonation.

We will use the effective charge Q_f^* as opposed to the nominal charge Q_f^{nm} and, as discussed in detail below, we will hypothesise that the difference between them is due to protonation (see Sec. S3.5).

S3.2. Ionic Coulomb blockade

For completeness, and for convenience of the reader, we now provide a brief description of the ICB model [14, 19, 25] of permeation and selectivity in biological ion channels. We follow fairly closely the Wikipedia article "Ionic Coulomb blockade".

ICB is a fundamental electrostatic phenomenon that emerges in the electro-diffusive transport of ions through narrow, low-capacitance channels, whether biological [14, 24, 26] or artificial [27, 28]. ICB predicts Q_f (or Q_F^*) to be an important determinant of selectivity, and one that is manifested strongly for divalent ions e.g. by giving rise to Ca^{2+} conduction bands [13]. ICB is closely analogous to its electronic ($z = -1$) counterpart in quantum dots [29, 30] and nanostructures[28, 31]. Coulomb blockade can be also seen in superconductors, where the charge carriers are Cooper pairs ($z = -2e$) [32].

The initial (basic) ICB model for the permeation and selectivity of ion channels [24] has recently been enhanced [33, 34] by the introduction of shift/corrections to allow for the singular part of the ionic attraction to the binding site (i.e. local site-binding), as well as for the effect of the ion's excess chemical potential $\Delta\mu$. The geometry-dependent shift of the ICB calcium resonant point resulting from these corrections leads to a change in the divalent (calcium) blockade threshold IC_{50} [19].

The model is well-fitted to describing the voltage-gated bacterial sodium channels NaChBac, NavAb, NavMs, and NvsBa. Because they are a family of relatively simple channels with discovered structures, they are widely used in modelling the general features of conductivity and selectivity [35–43].

We consider the stochastic transport of fully-hydrated ions of valence z having charge $q = ze$ (e.g. Ca^{2+} with $z = 2$). As indicated above, resonant barrier-less conduction arises when the energy of the ion-site attraction U_{gQ} is balanced by the dielectric self-energy barrier U_q^{SE} [14, 20, 21]. The ICB model allows us to derive the channel/ion parameters satisfying the barrier-less permeation conditions, and to do so from basic electrostatics taking account of charge discreteness.

The ICB balance equation can be derived using the ion's chemical potential μ [24], together with the 1D quadratic form of the SF Coulomb energy U_{SF} [7, 24, 27]:

$$U_{SF} = \frac{Q_{SF}^2}{2C_s}; \quad Q_{SF} = \sum_i q_i + Q_f = zne + Q_f, \tag{S1}$$

where Q_{SF} is the net charge of the SF and C_s is its self-capacitance, and n is the number of identical ions inside the SF. The sign of the charge q_i of the moving ions is opposite to that of the fixed charge Q_f. Statistical mechanics [44, 45] tells us that, in thermal and particle equilibrium with the bulk reservoirs, the entire system has a common μ_F (the *Fermi level*, in other contexts). An immediate consequence is the existence of an oscillatory dependence of conduction on Q_f, with two interlaced sets of singular points:

(i) Coulomb blockade points $Q_f = Z_n$, corresponding to neutralised states of the SF, with $Q_{SF} = 0$;

(ii) Resonant conduction points $Q_f = M_n$, corresponding to barrier-less conduction states, with $\Delta U_q = 0$ being the height of the energy barrier impeding passage of the ion through the channel.

The conditions for these singularities are

$$\begin{aligned} Z_n^{ICB} &= -zne \qquad \text{(Blockade points)} \\ M_n^{ICB} &= -ze(n + 1/2) \qquad \text{(Barrierless points)} \end{aligned} \tag{S2}$$

where $\{n\}$ is the number of ions captured in the SF before the transition. Note the predicted independence of channel structure and dimensions, validated in earlier BD simulations [13].

That is the main ICB result: for $z > 1$ the current *vs.* Q_f exhibits *Coulomb blockade oscillations* between zero-conduction blockade points Z_n at one extreme, and resonant barrier-less M_n points at the other. The oscillations in current I correspond to a *Coulomb staircase* in the channel/SF occupancy P_c.

Fig. S6 shows the BD-simulated I and P_c for Na^+ in panels (a),(b) and for Ca^{2+} in (c),(d) as functions of Q_f for different ionic concentrations, thus confirming and illustrating the main ICB phenomena. Panel (a) shows weak Na^+ ($z = 1$) conduction oscillations between resonant maxima and partially-blockaded reduced-conduction points. Panel (b) shows the corresponding smoothed-out Coulomb staircase of channel occupancy. In contrast, panel (c) illustrates the strong conduction bands observed for Ca^{2+} ($z = 2$), i.e.

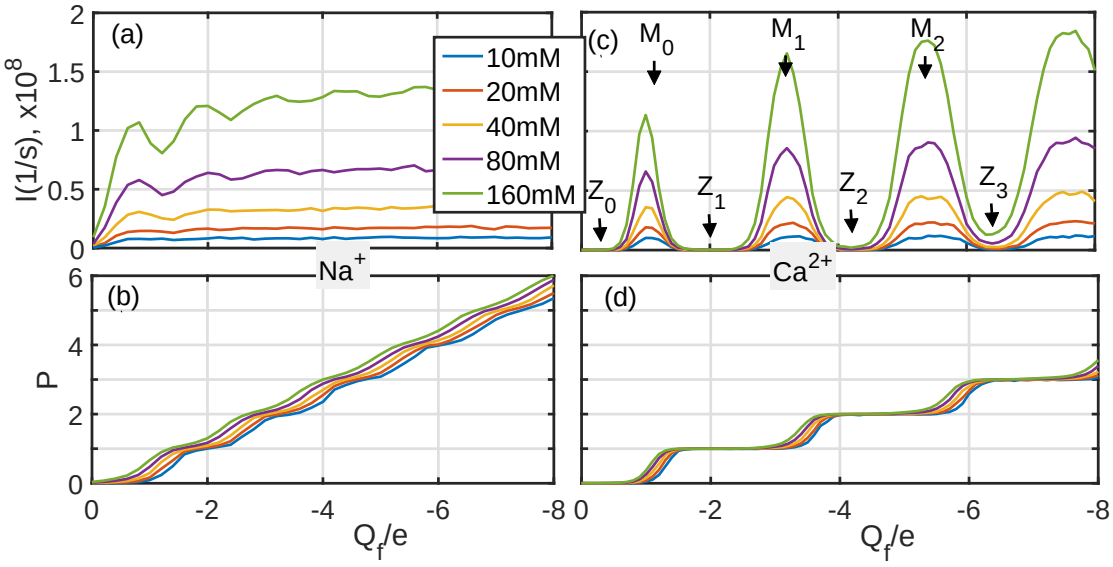

Figure S 6: Brownian dynamics simulations of multi-ion conduction and occupancy for Na^+ (left column) and Ca^{2+} (right column) ions in the model of Fig. S5 as the fixed charge Q_f is varied. In (a),(b) pure Na^+ baths of different concentration were used, at 10, 20, 40, 80 and 160mM as indicated; in (c),(d) pure Ca^{2+} solutions of the same concentrations were used. (a) Weak conduction oscillations in the Na^+ current I (permeation events per second) can be seen. (b) The Na^+ occupancy P shows a washed-out Coulomb staircase with clear evidence for concentration-related shifts. (c) The strong Coulomb blockade oscillations in the Ca^{2+} current also exhibit concentration-related shifts. The conduction bands at M_n, and the blockade/neutralisation points at Z_n, are discussed in the text. (d) The Ca^{2+} occupancy P forms a well-defined Coulomb staircase, again with concentration-related shifts. (Reworked from [19])

oscillations between resonant points M_n and blockaded points Z_n. The corresponding occupancy plot (d) for Ca^{2+} is a well-defined Coulomb staircase in occupancy P_c.

These phenomena provide for selectivity of the current. The peak conduction positions for different ionic species are shifted relative to each other, thus defining the responses of particular channels (with given Q_f) to particular ions or conditions. And *vice versa*, ICB oscillations (conduction bands) along Q_f^* provide a general and transparent explanation of the mutation-related transformations of selectivity [9, 13]. As illustrated, such ICB effects are expected to manifest themselves weakly for monovalent ions (e.g. Na^+), strongly for divalent ions (e.g. Ca^{2+}), and very strongly for trivalent ions (e.g. La^{3+}).

The strong oscillations in the Ca^{2+} current can serve as a basis for mapping Q_f^* onto particular mutant channels: we assume that Ca^{2+} stop bands Z_n correspond to Na^+-selective channels (non-conducting for Ca^{2+}), whereas Ca^{2+}-selective channels operate at Ca^{2+} resonant points M_n ([9, 14]).

The shapes of ICB-based Coulomb staircases for P_c are described by a Fermi-Dirac (FD) function of Q_f, of the charging energy ΔU_q, or of the logarithm of concentration [14, 24]:.

$$P_c = \left(1 + P_b^{-1} \exp\left(\frac{\Delta U_q}{k_B T}\right)\right)^{-1} \tag{S3}$$

where the equivalent bulk occupancy P_b is related to the bulk concentration and the volume of the SF. This prediction has been confirmed directly by divalent blockade/AMFE experiments [19].

The applicability of FD statistics Eq. (S3) to classical stochastic systems obeying an exclusion principle was demonstrated rigorously by **(author?)** [46]. The same FD statistics will be applied below to site protonation.

ICB (see Equation (S1) and Fig. S6) leads automatically to the strong claim that Q_f is the main determinant of selectivity in the calcium/sodium channels family. It also explains the famous and puzzling

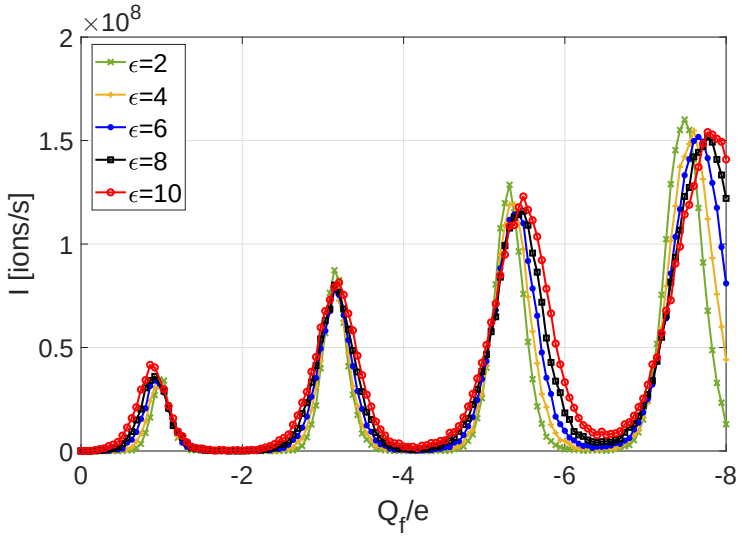

Figure S 7: Brownian dynamics simulations for Ca^{2+} ions in the model of Fig. S5 as the fixed charge Q_f is varied, for 5 different values of ε_p, as shown, while keeping all other parameters fixed.

transformations of Na^+-selective channels to Ca^{2+}-selective ones with increase of $|Q_f^{nm}|$ and *vice versa* [36, 47, 48].

Addition of the partial excess chemical potentials $\Delta\mu$ coming from different sources Y [2, 45, 49] to the ICB barrier-less condition $\Delta\mu = 0$ shifts the ICB resonant points M_n, as described by a "shift equation" [19, 33, 34] which, for $n = 0$, is

$$\Delta M_0 = M_0 - M_0^{ICB} = -\frac{C_s}{q}\sum_Y \Delta\mu^Y . \tag{S4}$$

The more important of these shifts (excess potentials) are:

- A concentration-related shift $\Delta\mu^{TS} = -k_B T \log(P_b)$ arising from the bulk entropy[45].
- A quantised dehydration-related shift $\Delta\mu^{DH}$ which we describe in section S3.4.

S3.3. Parametric tests of the model

The model is applicable to long, narrow, water-filled, channels where there is a large dielectric mismatch between the permittivities of the water and of the protein walls. Under these conditions, the electric field in the channel can be approximated as one-dimensional [50] because the field lines hardly enter the protein. The parameter range within which this approximation remains valid was explored earlier [13] in relation to the geometry (length L_c and radius R_c) of the pore; we now consider the effect of variations in the protein permittivity ε_p while holding the permittivity of the water ε_w fixed at its bulk value of 80.

Fig. S7 shows the results of Brownian dynamics simulations in which the permeating current is plotted as a function of Q_f for five different values of ε_p, while keeping all other parameters fixed, with $L_c = 10.0$Å, $R_c = 3.0$Å, and concentration 160 mM. We note that the results are relatively insensitive to large changes in ε_p. In particular, despite small discrepancies attributable to field penetration into the protein for $\varepsilon_p = 10$ (i.e. following a change of a factor of 5×), the blockade points Z_n barely move, thus validating the ICB approximation.

S3.4. Resonant quantised dehydration model

Dehydration, either full or partial, is thought to be the main source of selectivity between equally charged ions, e.g. monovalent alkali metal ions [6, 8, 51, 52]. The basic ICB model takes account of hydration/dehydration only through the dielectric self-energy U_q^{SE} in a 1D Coulomb approximation [7, 8] which is independent of the size of the ion, so additional effects need to be included in the model.

One such effect is the discreteness of the hydration shells, which strongly influences selectivity [8, 21, 53, 54]. Details of the ion-ligand interactions [54–56] and multi-ion knock-on mechanisms [3, 57] are also important. A hydrated ion is assumed to be surrounded by spherical, discrete, single-molecule-thick water shells of equal radial thickness h_c. The first shell is immediately adjacent to the ion, so the hydrated ion moves as an ion-water complex of radius

$$R^*_{ion} = R_{ion} + h_c. \tag{S5}$$

The shell model of hydration has been well validated by experimental, analytical and numerical evidence. So, consistent with the positions of the minima observed in experimental and MD-simulated radial density functions [53, 58], we will take $h_c = 0.2\,\text{nm}$ for monovalent ions and $h_c = 0.225\,\text{nm}$ for divalent ions.

During their passage through the SF, ions lose/rearrange their first hydration shells, with corresponding energy penalties: while small rearrangements of the shell are relatively cheap energetically, a decrease in the coordination number immediately leads to significant expense [54]. Generic (Q_f-independent) shell-based QD models provide a simple explanation for the difference in K^+/Na^+ selectivity between K^+ and Na^+/Ca^{2+} channels [8, 53, 54]:

- Within narrow K^+ channels, both Na^+ and K^+ ions are fully dehydrated. The first hydration shell is more tightly-bound to the smaller Na^+ ion, $\Delta\mu_K^{DH} < \Delta\mu_{Na}^{DH}$, and so the channel (counter-intuitively) favours the larger ion. Recent study has emphasised the role of direct Coulomb knock-on in the high K^+/Na^+ selectivity of K^+ channels [59].
- In contrast, the moderately wide Na^+ or Ca^{2+} channels accommodate both Na^+ and K^+ ions with their first hydration shells intact. Hence, $\Delta\mu_K^{DH} > \Delta\mu_{Na}^{DH}$ and the channel (more intuitively) favours the smaller Na^+ ion.

(author?) [53] have suggested a simple model of QD energetics based on consideration of hydration shells as thin spherical layers, calculation of the hydration energies of Born shells, and summing over shells. The energy of the first shell U_1^{DH} is found to be

$$U_1^{DH} \approx \frac{q^2}{8\pi\epsilon_0}\left(\frac{1}{\varepsilon_p} - \frac{1}{\varepsilon_w}\right)\left(\frac{1}{R_{ion}} - \frac{1}{R^*_{ion}}\right) \tag{S6}$$

In this model, an energy barrier appears due to the stripping-off of a fraction f_s of the first-shell's spherical surface R^*_{ion} remaining *outside* the pore of effective radius R_c:

$$\Delta^{DH} = (1-f)U_1^{DH}; \qquad f = 1 - \sqrt{1-(R_c/R^*_{ion})^2} \tag{S7}$$

However, neither the generic model, nor Zwolak's QD variant of it, consider the influence of Q_f on the selectivity sequences of a channel. To do so, we now combine the ideas of the QD models [8, 53, 54] with the Eisenman-inspired model of barrier-less selectivity [20, 21, 60] and, in particular, with the enhanced ICB model [14, 33, 34].

We consider an ion that retains its first shell almost untouched during its passage through the SF, so that it remains partially hydrated. In the picture proposed, the difference in $\Delta\mu^{DH}$ is not enough *per se* to determine which species will be selected over the other as this choice could be changed or even inverted by the value of Q_f needed to provide barrier-less conduction, i.e. through the corresponding shift of the resonant point M_n. Hence, if $\Delta\mu^{DH}$ increases with R_{ion} then $|M_n|$ will also increase for Na^+/Ca^{2+} channels, (though *vice versa* it will decrease for the narrower K^+ channels).

We assume that, for Na^+/Ca^{2+} channels, the huge difference in dielectric constant between water and protein ($\varepsilon_w \gg \varepsilon_p$) means that the electrostatic field W of an ion inside the channel can be decomposed in

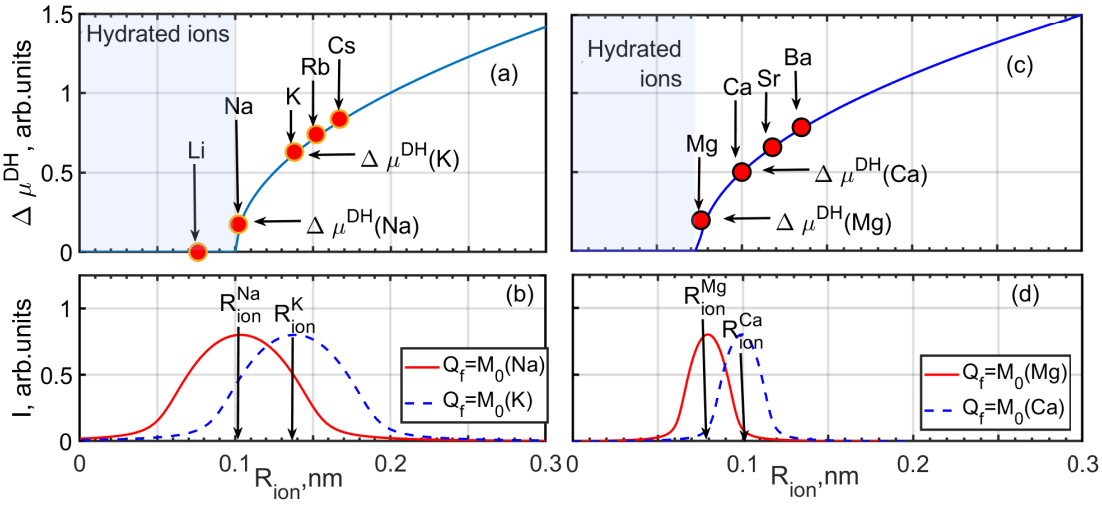

Figure S 8: Quantised dehydration scheme for monovalent (a,b) and divalent (c,d) ions in the selectivity filter (SF) of the NaChBac channel. The radius of the SF is taken as $R_c = 0.3\,\text{nm}$, and the thickness of the first hydration shell as $h_c \approx 0.2\,\text{nm}$. (a,c) The dehydration part of excess chemical potential $\Delta\mu_q^{DH}$ *vs.* R_{ion} is shown by the blue solid line. The shaded areas indicate the range of radii where ions can fit within the SF while still retaining their 1st hydration shells intact. (b,d) The conduction current I *vs.* R_{ion} for fixed charge Q_f equal to the first resonance M_0 for different ions, as indicated.

terms of a small parameter $\kappa = \varepsilon_p/\varepsilon_w$ as:

$$W = W^{ICB} + W^{DH} = (1-\kappa)W^{ICB} + \kappa W^{SP} \tag{S8}$$

where W^{ICB} is the main 1D (flat) Coulomb field localized inside the channel and the "leaking field" W^{DH} is the spherical Coulomb field W^{SP} of the ion q attenuated by a factor of κ. The shell-based ionic free energy of dehydration, i.e. the dehydration part of the excess chemical potential $\Delta\mu_X^{DH}$, is calculated using the Zwolak approximation above for the energy of the first shell U_1^{DH} [8, 53]:

$$\Delta\mu_X^{DH} = \kappa U_1^{DH} f_s \propto \kappa\sqrt{R_{ion}^* - R_c} \tag{S9}$$

where $X = \{K, Na, Ca...\}$. This result describes the dehydration-related shift in the selectivity of ion channels via the shift equation Eq. S4.

Fig. S8 (a) and (b) illustrate the basis of the QD picture for monovalent ions in the SFs of NaChBac and relevant mutants. The effective ionic radii R_{ion} are taken from [61]. The dehydration energy $\Delta\mu_q^{DH}$ (blue solid line) is calculated to be proportional to $\sqrt{R_{ion}^* - R_c}$, according to [8, 53]. The shaded area indicates the "fully hydrated" region where ions retain their 1st hydration shell untouched within the SF ($R_{ion}^* \leq R_c$). Plot (a) shows that Li^+ and Na^+ ions belong to the fully hydrated range of R_{ion}, whereas K^+, Rb^+ and Cs^+ lie on a rapidly rising part of the dehydration energy curve. Hence they require significant shifts in Q_f for the site affinity to balance the dehydration penalty in order to provide for barrier-less conduction. Plot (b) shows the current I_{ion} *vs.* R_{ion} plotted for values of Q_f that show resonances for Na^+ and K^+, respectively. Monovalent ions are described by relatively wide resonance curves, typical of weak ICB [9, 14].

Fig. S8 (c) and (d) show the corresponding plots for divalent ions. Plot (c) shows that the Mg^{2+} ion belongs to the "fully hydrated" range of R_{ion}, whereas Ca^{2+}, Sr^{2+} and Ba^{2+} all require shifts in Q_f to provide for barrier-less conduction. Plot (d) shows current I_{ion} *vs.* R_{ion} curves for values of Q_f, showing resonances for Mg^{2+} and Ca^{2+}, respectively. The results and predictions are rather similar to those for monovalent ions but with the much narrower resonances typical of strong ICB [9, 14], corresponding to the stronger dependence of conduction on ionic radius.

In summary, after inclusion of resonant QD effects, the resultant ICB/QD model predicts the following dependences of a channel's selectivity on Q_f, channel radius R_c and ion size R_{ion}:

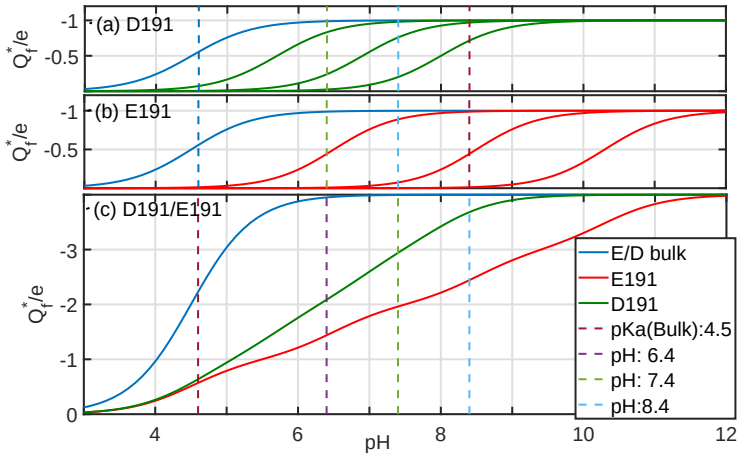

Figure S 9: Sketch of the putative protonation scheme for the D191 and E191 sites in NaChBac.

Narrow channels ($R_c \approx 0.2\,$nm e.g. KcsA channel) conduct fully dehydrated ions. These channels tend to favour larger ions (K^+) ([8, 54]). When Q_f is varied, narrow channels follow the original Eisenman rule, i.e. a highly charged ("high field strength") SF tends to favour small ions [20] and *vice-versa*. The origin of these shifts lies in the decrease in dehydration energy with growth of R_{ion}.

Moderately-wide channels ($R_c \approx 0.3 - 0.4\,$nm, e.g. NaChBac, NavAb, or Ca) conduct ions that retain significant parts of their first hydration shells. Low-charged mutants can then resonantly conduct small (Li^+ and Na^+) ions and the growth of $|Q_f|$ leads to an *inverse* shift of Eisenman sequence toward the larger ions, i.e. $Na^+ \rightarrow K^+$. This result arises from an increase in dehydration energy with growth of R_{ion}, when more water molecules have to change their positions/orientations (see Eq. S9).

(author?) [55] suggested an alternative (speculative) explanation of the influence of Q_f on K^+ *vs.* Na^+ selectivity in terms of a "asymmetrical snug fit" the ion to the pore. That explanation does not, however, provide an explicit dependence of the selectivity on Q_f and nor can it be tested in experiment.

S3.5. Protonation of residues in EEEE/DDDD rings

Protonation is to be anticipated in the confined space within the SF; and possible protonation of the EEEE locus has been under consideration for many years [6, 9, 62]

A titration curve that defines the ionisation of residues *vs.* pH can be derived from exactly the same considerations as we used in our derivation of the Coulomb staircase. In the simplest case of non-interacting residues R_i, the ionisation/protonation kinetics based on ionisation energy ΔE_{ion} [63, 64] results in FD statistics for the probability θ of ionisation (and charge Q_f), usually written as a Henderson- Hasselbalch equation [63, 65]:

$$\begin{aligned} \theta &= \left(1 + 10^{(pK_a - pH)}\right)^{-1}; \\ Q_f^* &= \theta Q_f^{nm}. \end{aligned} \tag{S10}$$

Taking account of the (repulsive) interaction energy ΔE_{int} between closely-spaced charges inside the charged rings will lead to sequential increases of effective ionisation energy for the second, third and forth residues in the ring and to a *composite* Coulomb staircase titration curve (i.e. the sum of elementary titration curves with different pK_a) [65, 66], similar to the occupancy dependence for monovalent ions like Na^+, and to a shift $\Delta(pK_a)$ in the iso-electric point of the protein.

Fig. S9 shows a sketch of the hypothesised ionisation/protonation scheme for the D191 and E191 sites, compatible with the observed selectivity and AMFE results. Both the DDDD and EEEE rings show significant interaction between charges, resulting in deviation of the titration curves from standard $pK_a \approx 4.0$

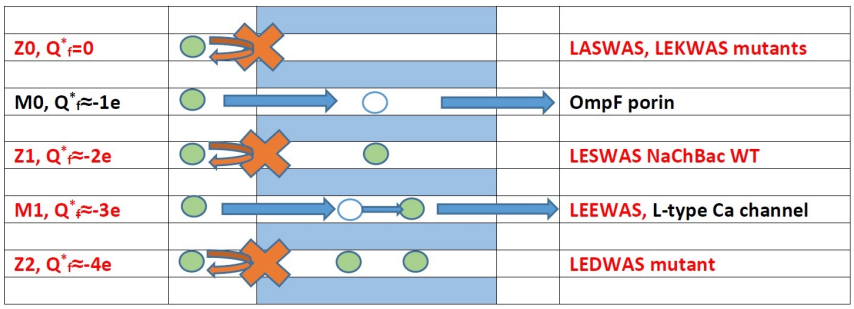

Figure S 10: Transformation of the Ca^{2+} conduction mechanism with increasing absolute value of effective fixed charge $|Q_f^*|$, showing the Coulomb blockade oscillations of multi-ion conduction/blockade states. The neutralized states Z_n providing blockade are interleaved with resonant conduction states M_n. The $|Q_f^*|$ value increases from top to bottom, as shown. Green circles indicate Ca^{2+} ions, unfilled circles show vacancies (virtual empty states used during permeation). The right-hand column indicates the preliminary identifications of particular channels/mutants corresponding to particular mechanisms. The mutants studied here are shown in red. (Modified from [19])

values. Following **(author?)** [65] we approximate the titration curves for the D191 and E191 residues rings as sums of four individual curves with different pK_a, these putative decompositions are shown in plot (a) for DDDD and plot (b) for EEEE. Glutamate residues in the EEEE ring are significantly protonated ($pK_a \approx 7$) and hence the effective Q_f at pH=7.4 is about $-2e$, whereas the DDDD ring has $Q_f = -3e$ ($pK_a \approx 6$). In (c) the curves sketched are composite Coulomb staircases corresponding to sets $pK_a(i)$={4.5, 6.5, 8.5, 10.5} for EEEE and $pK_a(i)$={4.5, 5.7, 6.9, 8.0} for DDDD. This picture provides an explanation for all the observations including, in particular, the results of divalent blockade experiments.

S4. Results

S4.1. Q_f^*-mapping table

Table S 5: Divalent blockade and Q_f^* - mapping. The table presents the results of divalent blockade experiments with NaChBac site-directed mutants of different nominal charge Q_f^{nm}, such as logarithmic blockade threshold $\log IC_{50}$; together with estimated values of the effective charge Q_f^* and the corresponding ICB points M_n, Z_n.

Mutant	Q_f^{nm}/e	$\lg(IC_{50}), M$	Q_f^*/e	ICB point
LASWAS	0		0	Z_0
LESWAS	-4	-1.7	-2	Z_1
LDSWAS	-4	-2.9	≈-2.4	
LEEWAS	-8	-4.8	≈-3.1	$\approx M_1$
LEDWAS	-8	-5.3	≈-3.3	
LDEWAS	-8	-7	-4	Z_2
LDDWAS	-8	-8	≈-4.4	

S4.2. ICB/Protonation-based conduction vs Q_f^* scheme for real channels/mutants

The protonation-related model presented above leads to a significant decrease in the effective values $|Q_f^*|$ in comparison with the nominal values $|Q_f^{nm}|$ of the fixed charge, and, hence to a modification of the earlier identification scheme [19]. The current scheme is built around strong Ca^{2+} ICB oscillations (see Fig. S6(c)). It is based on the Ca^{2+} Z_n and M_n points and on the Q_f^* values obtained here with account taken of protonation.

Figure S10 presents in diagrammatic form the quasi-periodic sequence of multi-ion blockade/conduction modes arising from growth of $\{n\}$ as Q_f^* increases, together with putative identifications of particular modes and of the NaChBac mutants used in this work. The diagram is based on the data shown in Table. S5 and Fig. S6.

- The state Z_0 with $Q_f^* = 0$ represents ICB for the empty selectivity filter, brought about by image forces – as observed experimentally in LASWAS (see above) and also in artificial nanopores [28].
- The joint Ca^{2+}/Na+ resonant point M_0/M_1 corresponds to single-ion (i.e. $\{n\} = 1$) barrier-less Ca^{2+} conduction, and can putatively be related to the OmpF porin [9, 67].
- The Ca^{2+} Z_1 channel corresponds to WT LESWAS with single-ion block of the Ca^{2+} current. WT NaChBac channel conducts sodium and does not conduct calcium.
- The Ca^{2+} M_1 state corresponds to double-ion knock-on, and may be identified with the LEEWAS mutant and (putatively) with L-type calcium channel having EEEE locus and additional charged D residue in the neighbouring position [19, 68].
- The LEDWAS mutant ($Q_f^* = -4e$) can be identified with the Z_2 Ca^{2+} blockade point, such an identification being supported both by BD simulations and by patch-clamp studies.

References

[1] Hille, B., *Ion Channels Of Excitable Membranes* (Sinauer Associates, Sunderland, MA, 2001), 3rd edn.

[2] Roux, B., Allen, T., Berneche, S. & Im, W., Theoretical and computational models of biological ion channels, *Quart. Rev. Biophys.* **37**, 15–103 (2004).

[3] Bernèche, S. & Roux, B., Energetics of ion conduction through the K^+ channel, *Nature* **414**, 73–77 (2001).

[4] Corry, B., Allen, T. W., Kuyucak, S. & Chung, S. H., Mechanisms of permeation and selectivity in calcium channels, *Biophys. J.* **80**, 195–214 (2001).

[5] Boda, D., Nonner, W., Henderson, D., Eisenberg, B. & Gillespie, D., Volume exclusion in calcium selective channels, *Biophys. J.* **94**, 3486–3496 (2008).

[6] Nonner, W. & Eisenberg, B., Ion permeation and glutamate residues linked by Poisson-Nernst-Planck theory in L-type calcium channels, *Biophys. J.* **75**, 1287–1305 (1998).

[7] Zhang, J., Kamenev, A. & Shklovskii, B. I., Conductance of ion channels and nanopores with charged walls: A toy model, *Phys. Rev. Lett.* **95**, 148101 (2005).

[8] Laio, A. & Torre, V., Physical origin of selectivity in ionic channels of biological membranes, *Biophys. J.* **76**, 129–148 (1999).

[9] Kaufman, I. K., Luchinsky, D. G., Tindjong, R., McClintock, P. V. E. & Eisenberg, R. S., Energetics of discrete selectivity bands and mutation-induced transitions in the calcium-sodium ion channels family, *Phys. Rev. E* **88**, 052712 (2013).

[10] Owsianik, G., Talavera, K., Voets, T. & Nilius, B., Permeation and selectivity of TRP channels, *Annu. Rev. Physiol.* **68**, 685–717 (2006).

[11] Garcia-Fandiño, R. & Sansom, M. S. P., Designing biomimetic pores based on carbon nanotubes, *Proc. Natl. Acad. Sci. USA* **109**, 6939–6944 (2012).

[12] Miedema, H., Ion-selective biomimetic membranes, in *Biomimetic Membranes for Sensor and Separation Applications* (Ed. C. Hélix-Nielsen), pp. 63–86 (Springer, Dordrecht, 2012).

[13] Kaufman, I. K., Luchinsky, D. G., Tindjong, R., McClintock, P. V. E. & Eisenberg, R. S., Multi-ion conduction bands in a simple model of calcium ion channels, *Phys. Biol.* **10**, 026007 (2013).

[14] Kaufman, I. K., McClintock, P. V. E. & Eisenberg, R. S., Coulomb blockade model of permeation and selectivity in biological ion channels, *New J. Phys.* **17**, 083021 (2015).

[15] Nonner, W., Catacuzzeno, L. & Eisenberg, B., Binding and selectivity in l-type calcium channels: A mean spherical approximation, *Biophys. J.* **79**, 1976–1992 (2000).

[16] Giri, J., Fonseca, J. E., Boda, D., Henderson, D. & Eisenberg, B., Self-organized models of selectivity in calcium channels, *Phys. Biol.* **8**, 026004 (2011).

[17] Corry, B., Vora, T. & Chung, S. H., Electrostatic basis of valence selectivity in cationic channels, *Biochim. Biophys. Acta-Biomembranes* **1711**, 72–86 (2005).

[18] Kaufman, I. K., Tindjong, R., Luchinsky, D. G., McClintock, P. V. E. & Eisenberg, R. S., Resonant multi-ion conduction in a simple model of calcium channels, in *22nd Intern. Conf. on Noise and Fluctuations (ICNF),* Montpellier, 24–28 June 2013 (Eds. J. M. Routoure, L. Varani & F. Pascal), p. doi: 10.1109/ICNF.2013.6578926 (IEEE Conf. Proc., 2013).

[19] Kaufman, I. K., Fedorenko, O. A., Luchinsky, D. G., Gibby, W. A. T., Roberts, S. K., McClintock, P. V. E. & Eisenberg, R. S., Ionic Coulomb blockade and anomalous mole fraction effect in the NaChBac bacterial ion channel and its charge-varied mutants, *EPJ Nonlin. Biomed. Phys.* **5**, 1–8 (2017).

[20] Eisenman, G. & Horn, R., Ionic selectivity revisited: the role of kinetic and equilibrium processes in ion permeation through channels, *J. Membr. Biol.* **76**, 197–225 (1983).

[21] Yesylevskyy, S. O. & Kharkyanen, V. N., Barrier-less knock-on conduction in ion channels: peculiarity or general mechanism?, *Chem. Phys.* **312**, 127–133 (2005).

[22] Eisenberg, R. S., Ionic channels in biological membranes – electrostatic analysis of a natural nanotube, *Contemp. Phys,* **39**, 447–466 (1998).
[23] Zhang, J. & Shklovskii, B. I., Effective charge and free energy of DNA inside an ion channel, *Phys. Rev. E* **75**, 021906 (2007).
[24] Kaufman, I. K., Gibby, W. A. T., Luchinsky, D. G., McClintock, P. V. E. & Eisenberg, R. S., Coulomb blockade oscillations in biological ion channels, in *Proc. 23rd Intern. Conf. on Noise and Fluctuations (ICNF), Xian*, p. doi: 10.1109/ICNF.2015.7288558 (IEEE Conf. Proc., 2015).
[25] Kaufman, I. K., Gibby, W. A. T., Luchinsky, D. G. & McClintock, P. V. E., Effect of local binding on stochastic transport in ion channels, *arXiv preprint arXiv:1704.00956* (2017).
[26] Kitzing, E., A novel model for saturation of ion conductivity in transmembrane channels, in *Membrane Proteins: Structures, Interactions and Models: Proceedings of the Twenty-Fifth Jerusalem Symposium on Quantum Chemistry and Biochemistry, Jerusalem, Israel, May 18-21,1992* (Eds. A. Pullman, J. Jortner & B. Pullman), pp. 297–314 (Springer Netherlands, Dordrecht, 1992).
[27] Krems, M. & Di Ventra, M., Ionic Coulomb blockade in nanopores, *J. Phys. Condens. Matter* **25**, 065101 (2013).
[28] Feng, J., Liu, K., Graf, M., Dumcenco, D., Kis, A., Di Ventra, M. & Radenovic, A., Observation of ionic Coulomb blockade in nanopores, *Nature Mater.* **15**, 850 – 855 (2016).
[29] Averin, D. V. & Likharev, K. K., Coulomb blockade of single-electron tunneling, and coherent oscillations in small tunnel junctions, *J. Low Temp. Phys.* **62**, 345–373 (1986).
[30] Beenakker, C. W. J., Theory of Coulomb-blockade oscillations in the conductance of a quantum dot, *Phys. Rev. B* **44**, 1646–1656 (1991).
[31] Grabert, H. & Devoret, M. H., *Single Charge Tunneling: Coulomb Blockade Phenomena in Nanostructures*, vol. 294 (Springer Science & Business Media, 2013).
[32] Amar, A., Song, D., Lobb, C. J. & Wellstood, F. C., 2e-periodic and e-periodic pair currents in superconducting Coulomb-blockade electrometers, *Phys. Rev. Lett* **72**, 3234–3237 (1994).
[33] Kaufman, I. K., Gibby, W. A. T., Luchinsky, D. G. & McClintock, P. V. E., Effect of local binding on stochastic transport in ion channels, in *2017 Intern. Conf. on Noise and Fluctuations* 10.1109/ICNF.2017.7985974, pp. 1–4 (2017).
[34] Luchinsky, D. G., Gibby, W. A. T., Kaufman, I. K., McClintock, P. V. E. & Timucin, D. A., Relation between selectivity and conductivity in narrow ion channels, in *2017 International Conference on Noise and Fluctuations (ICNF)*, p. DOI: 10.1109/ICNF.2017.7985973 (2017).
[35] Ren, D. J., Navarro, B., Xu, H. X., Yue, L. X., Shi, Q. & Clapham, D. E., A prokaryotic voltage-gated sodium channel, *Science* **294**, 2372–2375 (2001).
[36] Yue, L. X., Navarro, B., Ren, D. J., Ramos, A. & Clapham, D. E., The cation selectivity filter of the bacterial sodium channel, NaChBac, *J. Gen. Physiol.* **120**, 845–853 (2002).
[37] DeCaen, P. G., Takahashi, Y., Krulwich, T. A., Ito, M. & Clapham, D. E., Ionic selectivity and thermal adaptations within the voltage-gated sodium channel family of alkaliphilic Bacillus, *eLife* **3**, e04387 (2014).
[38] Finol-Urdaneta, R. K., Wang, Y., Al-Sabi, A., Zhao, C., Noskov, S. Y. & French, R. J., Sodium channel selectivity and conduction: prokaryotes have devised their own molecular strategy, *J. Gen. Physiol.* **143**, 157–171 (2014).
[39] Naylor, C. E., Bagnéris, C., DeCaen, P. G., Sula, A., Scaglione, A., Clapham, D. E. & Wallace, B. A., Molecular basis of ion permeability in a voltage-gated sodium channel, *EMBO J.* **35**, 820–830 (2016).
[40] Guardiani, C., Rodger, P. M., Fedorenko, O. A., Roberts, S. K. & Khovanov, I. A., Sodium binding sites and permeation mechanism in the NaChBac channel: A molecular dynamics study, *J. Chem. Theor. Comput.* **13**, 1389–1400 (2017).
[41] Guardiani, C., Fedorenko, O. A., Roberts, S. K. & Khovanov, I. A., On the selectivity of the NaChBac channel: an integrated computational and experimental analysis of sodium and calcium permeation, *Phys. Chem. Chem. Phys.* **19**, 29840–29854 (2017).
[42] Catterall, W. A., Wisedchaisri, G. & Zheng, N., The chemical basis for electrical signaling, *Nature Chem. Biol.* **13**, 455–463 (2017).
[43] Payandeh, J. & Minor, D. L., Bacterial voltage-gated sodium channels (BacNaVs) from the soil, sea, and salt lakes enlighten molecular mechanisms of electrical signaling and pharmacology in the brain and heart, *J. Mol. Biol.* **427**, 3–30 (2015).
[44] Landsberg, P. T., *Thermodynamics and Statistical Mechanics* (Courier Corporation, 2014).
[45] Krauss, D., Eisenberg, B. & Gillespie, D., Selectivity sequences in a model calcium channel: role of electrostatic field strength, *Eur. Biophys. J.* **40**, 775–782 (2011).
[46] Kaniadakis, G. & Quarati, P., Kinetic equation for classical particles obeying an exclusion principle, *Phys. Rev. E* **48**, 4263–4270 (1993).
[47] Heinemann, S. H., Teriau, H., Stuhmer, W., Imoto, K. & Numa, S., Calcium-channel characteristics conferred on the sodium-channel by single mutations, *Nature* **356**, 441–443 (1992).
[48] Ellinor, P. T., Yang, J., Sather, W. A., Zhang, J.-F. & Tsien, R. W., Ca^{2+} channel selectivity at a single locus for high-affinity Ca^{2+} interactions, *Neuron* **15**, 1121–1132 (1995).
[49] Boda, D., Henderson, D. & Gillespie, D., The role of solvation in the binding selectivity of the L-type calcium channel, *J. Chem. Phys.* **139**, 055103 (2013).
[50] Zhang, J., Kamenev, A. & Shklovskii, B. I., Ion exchange phase transitions in water-filled channels with charged walls, *Phys. Rev. E* **73**, 051205 (2006).
[51] Sahu, S., Di Ventra, M. & Zwolak, M., Dehydration as a universal mechanism for ion selectivity in graphene and other atomically thin pores, *Nano Lett.* **17**, 4719–4724 (2017).
[52] Li, K., Tao, Y., Li, Z., Sha, J. & Chen, Y., Selective ion-permeation through strained and charged graphene membranes,

Nanotech. **29**, 035402 (2017).
[53] Zwolak, M., Lagerqvist, J. & Di Ventra, M., Quantized ionic conductance in nanopores, *Phys. Rev. Lett.* **103**, 128102 (2009).
[54] Corry, B., Mechanisms of selective ion transport and salt rejection in carbon nanostructures, *MRS Bull.* **42**, 306–310 (2017).
[55] Corry, B. & Thomas, M., Mechanism of ion permeation and selectivity in a voltage gated sodium channel, *J. Amer. Chem. Soc.* **134**, 1840–1846 (2012).
[56] Dudev, T. & Lim, C., Evolution of eukaryotic ion channels: Principles underlying the conversion of Ca^{2+}-selective to Na^{+}-selective channels, *J. Amer. Chem. Soc.* **136**, 3553–3559 (2014).
[57] Hodgkin, A. L. & Keynes, R. D., The potassium permeability of a giant nerve fibre, *J. Physiol.* **128**, 61–88 (1955).
[58] Shao, Q., Zhou, J., Lu, L., Lu, X., Zhu, Y. & Jiang, S., Anomalous hydration shell order of Na^{+} and K^{+} inside carbon nanotubes, *Nano Lett.* **9**, 989–994 (2009).
[59] Kopec, W., Köpfer, D. A., Vickery, O. N., Bondarenko, A. S., Jansen, T. L., de Groot, B. L. & Zachariae, U., Direct knock-on of desolvated ions governs strict ion selectivity in K^{+} channels, *Nat. Chem.* **10**, 813–820 (2018).
[60] Nadler, B., Hollerbach, U. & Eisenberg, R. S., Dielectric boundary force and its crucial role in gramicidin, *Phys. Rev. E* **68**, 021905 (2003).
[61] Shannon, R. D., Revised effective ionic radii and systematic studies of interatomic distances in halides and chalcogenides, *Acta Cryst. A* **32**, 751–767 (1976).
[62] Chen, X.-H. & Tsien, R. W., Aspartate substitutions establish the concerted action of P-region glutamates in repeats I and III in forming the protonation site of L-type Ca^{2+} channels, *J. Biol. Chem.* **272**, 30002–30008 (1997).
[63] Job, G. & Rüffler, R., *Physical Chemistry from a Different Angle* (Springer, 2016).
[64] Woodhull, A. M., Ionic blockage of sodium channels in nerve, *J. Gen. Physiol.* **61**, 687–708 (1973).
[65] Onufriev, A., Case, D. A. & Ullmann, G. M., A novel view of pH titration in biomolecules, *Biochem.* **40**, 3413–3419 (2001).
[66] Bezrukov, S. M. & Kasianowicz, J. J., Current noise reveals protonation kinetics and number of ionizable sites in an open protein ion channel, *Phys. Rev. Lett.* **70**, 2352 (1993).
[67] Miedema, H., Meter-Arkema, A., Wierenga, J., Tang, J., Eisenberg, B., Nonner, W., Hektor, H., Gillespie, D. & Meijberg, W., Permeation properties of an engineered bacterial OmpF porin containing the EEEE-locus of Ca^{2+} channels, *Biophys. J.* **87**, 3137–3147 (2004).
[68] Kaufman, I. K., Luchinsky, D. G., Gibby, W. A. T., McClintock, P. V. E. & Eisenberg, R. S., Putative resolution of the EEEE selectivity paradox in L-type Ca^{2+} and bacterial Na^{+} biological ion channels, *J. Stat. Mech.* **2016**, 054027 (2016).